

The Orbital Nature of Electron Holes in BaFeO₃ and Implications for Defect Chemistry

M. F. Hoedl,* C. Ertural, R. Merkle, R. Dronskowski, and J. Maier



Cite This: *J. Phys. Chem. C* 2022, 126, 12809–12819



Read Online

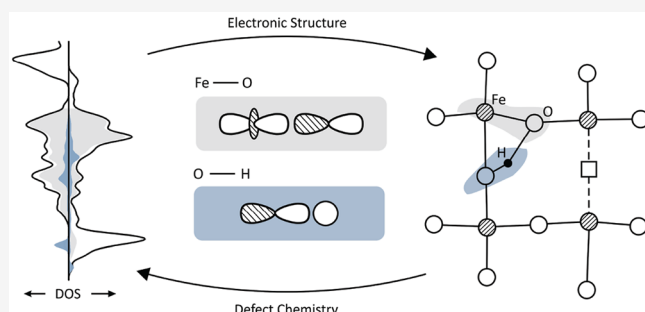
ACCESS |

Metrics & More

Article Recommendations

Supporting Information

ABSTRACT: Understanding the nature of electron holes in mixed protonic–electronic conducting perovskites is key to the successful development of novel electrode materials for protonic ceramic fuel and electrolyzer cells (PCFCs). Here, we use density functional theory to investigate the orbital interactions and defect chemistry of BaFeO_{3-δ}—a model material for more complex cation stoichiometries used in PCFCs. The calculations revealed BaFeO_{3-δ} to be a negative charge-transfer material with a dominating d⁵L (L = ligand hole) configuration. Chemical bonding analysis using the projected Crystal Orbital Hamilton Population (COHP) further showed that the ligand holes are partially delocalized in pdσ* bonds with an approximately 80% share at the oxygen ions. The defect chemistry of BaFeO₃ was explored with respect to oxygen vacancies and protonic defects. The oxygen vacancy formation energy increases with decreasing ligand hole concentration due to a rising Fermi level at which electrons from the removed oxygen are accommodated. This effectively outweighs a concomitant decrease in the Fe–O bond strength evidenced by energy-integrated COHP analysis. The dissociative H₂O absorption was studied, where OH⁻ fills an oxygen vacancy and H⁺ is attached to a regular oxygen ion. The energy of this reaction becomes more negative with decreasing ligand hole concentration. This trend largely reflects a more favorable OH⁻ affinity with decreasing ligand hole concentration.



1. INTRODUCTION

Owing to their variable and tunable composition, perovskites are prototypical materials for the investigation of defect chemistry as well as key functional materials for many electrochemical applications.^{1–3} The perovskite BaFeO_{3-δ} belongs to the group of triple-conducting oxides with contributions from electron holes, mobile oxygen vacancies, and hydrogen ion (proton) interstitial defects.^{4–6} This unique functional property makes these materials promising electrode materials in fuel or electrolyzer cells that are based on proton-conducting ceramic electrolytes, providing both the necessary electronic conductivity to close the external circuit as well as fast reaction kinetics enabled by the ionic conductivity. The doping and cation composition of triple-conducting perovskites have been extensively studied in recent years to understand general trends in the various charge carrier concentrations.^{4–6} Interestingly, it turned out that ionic charge carriers and electron holes exhibit profound interactions that have a direct impact on the applications. However, the nature of these interactions is still poorly understood and is the subject of the present study.

BaFeO_{3-δ} in the cubic perovskite structure can be regarded as the undoped parent system serving as model material for more complex cation compositions. BaFeO_{3-δ} exhibits thermally activated electronic conductivity on the order of 1–10 S/cm with an activation energy of 0.3 eV below 500 °C

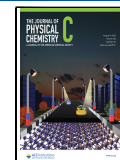
and ~−0.1 eV above 500 °C (decreasing hole concentration caused by increasing oxygen deficiency).⁷ The magnitude of the electronic conductivity increases with oxygen partial pressure, indicating that electron holes are the majority charge carriers. The electronic structure of BaFeO_{3-δ} is complex; nominal electron configurations of d⁴ (Fe⁴⁺) and p⁶ (O²⁻) suggest closed oxygen p shells and electron holes being associated with the Fe ions, rendering them redox-active species. X-ray spectroscopic studies on thin films and first-principles calculations, however, have consistently shown that the electronic ground state of cubic BaFeO₃ consists of a mixed d⁴ and d⁵L (L ligand hole) configuration, with a dominating d⁵L character.^{8–10}

Regarding the defect chemistry of BaFeO_{3-δ}, we focus on two types of point defects: oxygen vacancies and proton interstitial defects. Both are found to exhibit strong interactions with electron holes. This manifests in systematic variations of the defect formation energies as a function of the electron hole

Received: April 13, 2022

Revised: June 24, 2022

Published: July 21, 2022



concentration. For instance, in $\text{Ba}_{0.5}\text{Sr}_{0.5}\text{FeO}_3$, thermogravimetry experiments show that the oxygen vacancy formation enthalpy increases from 0.63 to 0.87 eV with increasing vacancy concentration from $\delta = 0$ to 0.5, hence decreasing the hole concentration¹¹ (see also refs 12 and 13). Similarly, measurements of $\text{Ba}_{1-x}\text{La}_x\text{FeO}_{3-\delta}$ show that proton uptake is significantly reduced in samples with higher hole concentrations.¹⁴ Moreover, doping with large, redox-inactive cations such as Zn^{2+} on the B site can massively increase proton uptake, e.g., from 3% in $\text{Ba}_{0.95}\text{La}_{0.05}\text{FeO}_{2.53}$ to 10% in $\text{Ba}_{0.95}\text{La}_{0.05}\text{Fe}_{0.8}\text{Zn}_{0.2}\text{O}_{2.4}$ under the same conditions,⁵ which was related to lattice distortions (Fe–O–Fe buckling) decreasing the hole delocalization.¹⁵

In this contribution, we provide a chemically intuitive description of the electronic structure of cubic BaFeO_3 and perform a quantitative analysis of the Fe–O chemical bond (section 4.1). We elaborate on the nature of the electron (ligand) holes, clarify the involved orbital interactions, and quantify the degree of hole delocalization between Fe and O. To elucidate the experimentally observed defect interactions, the thermodynamic parameters of oxygen vacancy formation and proton uptake as a function ligand hole concentration (cf. also ref 16) are analyzed in detail and correlated with changes in the electronic structure and bonding (section 4.2).

2. THEORETICAL METHODS AND COMPUTATIONAL DETAILS

The electronic structure and defect chemistry of cubic BaFeO_3 were studied using density functional theory (DFT). In particular, we used the pseudopotential-like DFT in conjunction with the projector augmented wave (PAW) method,¹⁷ as implemented in the Vienna Ab initio Simulation Package (VASP).^{18–20} In the DFT calculations, a constant energy cutoff of 500 eV was used. The structure was optimized until the electronic convergence criterion of 10^{-5} eV and the ionic criterion of residual forces below 10^{-4} eV/Å were met. The Brillouin zone of the 5-atom primitive unit cell was sampled with a $8 \times 8 \times 8$ Monkhorst–Pack^{21,22} k -point mesh. Exchange and correlation were treated with the Perdew–Burke–Ernzerhof (PBE) functional²³ with an additional on-site Hubbard-U interaction term²⁴ for the Fe 3d states of $U_{\text{eff}} = 4$ eV. As shown in ref 16, this value represents a good compromise between reproducing experimental values, e.g., of the magnetic moment, and falling in the range of U_{eff} values typically employed for Fe-containing perovskites (see, e.g., refs 25–27). To study point defects at low concentrations using periodic boundary conditions, the size of the unit cell must be increased into so-called supercells, as otherwise the defect concentrations would be unreasonably high. Here, point defects were modeled using a $2 \times 2 \times 2$ expansion of the primitive unit cell corresponding to a supercell of 40 atoms. The number of k points in the supercells was reduced accordingly. All calculations were performed for neutral supercells with full relaxation of the supercell dimensions (allowing also for, e.g., monoclinic distortion) and atomic coordinates. Regarding the calculation of gas-phase O_2 and H_2O , the molecules were placed into vacuum boxes of 12 Å edge lengths. The notorious overbinding in the O_2 molecule obtained with the PBE functional is corrected by adjusting the total energy by 1.36 eV, as suggested in the literature.²⁶

In general, the one-electron wave functions in DFT are commonly expressed in terms of a basis set, i.e., a linear combination of basis functions that can be constructed from

either atomic orbitals or plane wave-based functions. The plane wave part of the extended PAW wave functions used in VASP are naturally expressed by a plane wave basis set, which ensures high accuracy and efficiency in terms of computational speed. Despite this computational elegance, the totally delocalized nature of plane waves prevents a chemical interpretation of the electronic structure in terms of bonding and antibonding orbital interactions. To nonetheless allow for chemical bonding analysis, the optimized PAW wave functions were projected onto an auxiliary local basis set in a postprocessing step using the Local-Orbital Basis Suite Towards Electronic-Structure Reconstruction (LOBSTER) package, corresponding to a unitary delocalized-to-localized transformation in Hilbert space.^{28–34} To reconstruct the chemical information, different tools like projected COHP and fat-band analysis will be used in what follows.^{30,35} In this context, it is natural to use Mulliken population analysis to extract atomic charges directly from the wave function rather than a charge density partitioning according to Bader.^{32,34} The projected COHP essentially weighs the DOS of a pair of atomic orbitals by their corresponding off-site Hamiltonian matrix element to evaluate bonding, nonbonding, or antibonding interactions. In practice, the projected COHP is plotted as a function of the energy and is placed next to a DOS curve or (fat) band structure diagram, serving as a covalent bonding indicator. Three different cases can be distinguished.

- $\text{COHP}_{\mu\nu}(E) < 0$: The orbital interaction between a pair of atomic orbitals ($\mu\nu$) has a stabilizing effect on the energy, and consequently, the orbital interaction has a bonding character.
- $\text{COHP}_{\mu\nu}(E) = 0$: The interaction of the AOs under consideration has no impact on the energy, i.e., they are nonbonding.
- $\text{COHP}_{\mu\nu}(E) > 0$: A destabilizing effect of the orbital interaction and thus an antibonding interaction is indicated.

By sheer convention, the negative projected COHP is usually plotted such that states to the right (negative values) indicate bonding interactions and states to the left (positive values) indicate antibonding interactions. Finally, the energy-integrated COHP (ICOHP) up to the Fermi level yields a quantitative measure for the electronic energy associated with the chemical bond covalency. The results from Mulliken population analysis are discussed along other results as an ionic bond indicator.^{32,34}

3. CRYSTAL STRUCTURE AND SYMMETRY CONSIDERATIONS

BaFeO_3 adopts different crystal structures depending on the synthetic conditions. The most stable structure is hexagonal, featuring corner- and face-sharing $[\text{FeO}_6]$ octahedra, see Figure 1. However, a metastable cubic perovskite structure can be prepared under certain conditions,³⁶ to be regarded as a network of purely corner-sharing $[\text{FeO}_6]$ octahedra, with linear Fe–O–Fe arrangements. Here, the interstices between the octahedra are occupied by the larger barium cations, and each oxygen is in an axial coordination with two Fe as nearest neighbors (Figure 1). The optimized lattice parameter of the cubic unit cell yields a value of $a = 4.015$ Å, which is in good agreement with the experimental value of 3.97 Å, reported in refs 10, 36, and 37. Jahn–Teller effects in BaFeO_3 are discussed in the Supporting Information A.

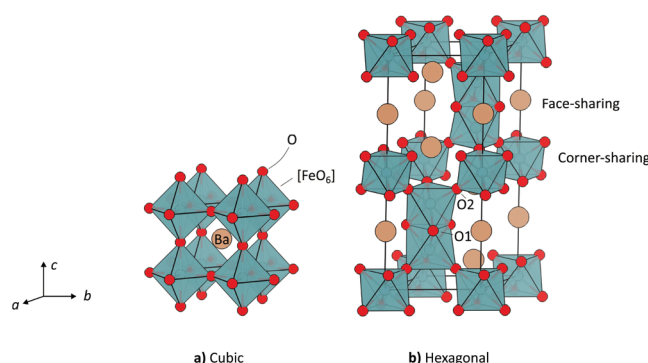


Figure 1. Crystal structures of different BaFeO_3 phases: red spheres, oxygen; brown spheres, barium; blue octahedra, $[\text{FeO}_6]$. The hexagonal structure refers to the 6H stacking sequence found for BaFeO_3 .³⁸ Different oxygen ion sites in the hexagonal structure are labeled O1 and O2.

The symmetry of the cubic perovskite structure places important constraints on the electronic structure: The d orbitals of Fe are split into t_{2g} and e_g levels, where electrons in the e_g orbitals experience a stronger repulsion by the negatively charged oxygen ions and consequently lie at higher energy as compared to electrons in the t_{2g} orbitals. On the other hand, oxygen ions have an axial coordination by two nearest-neighbor Fe, transforming the p orbitals of a given oxygen ion into a 2-fold degenerate set of p orbitals perpendicular to the $\text{Fe}-\text{O}-\text{Fe}$ axis and one p orbital parallel to that axis (referred to as p_\perp and p_\parallel orbitals). Electrons in the p_\parallel orbitals experience a stronger attraction by the positively charged Fe ions than electrons in the p_\perp orbitals, resulting in a lower energy of the p_\parallel orbitals than that of the p_\perp orbitals (Figure 2a). On the basis

Pauli's principle that two electrons of like spin cannot occupy the same position in space and thus experience a repulsion (exchange repulsion) between them. This translates into a reduced probability of finding like-spin electrons near each other. As a result, they shield the nuclear charge less effectively than electrons of opposite spin. In contrast, electrons with opposite spin do not experience exchange repulsion, so they approach each other more closely and thus shield the nuclear charge more effectively. Therefore, it is often energetically favorable for a system to adopt high-spin configurations to reduce the shielding of the nuclear charge and thus to increase the electron–nucleus attraction of the majority spin electrons. The increase in electron–nucleus attraction leads to more contracted orbitals of the majority spin electrons and corresponding lower energies. The reluctance of the system to doubly occupy the d orbitals and thereby to reduce the electron–nucleus attraction manifests in a gap between the spin-up and the spin-down orbitals. Eventually, this gap is codetermined by the intraorbital Coulomb repulsion between the electrons; the splitting is commonly abbreviated as U_{dd} .

Depending on the magnitude of the splitting, one can distinguish different regimes in the band structure: the Mott–Hubbard and negative charge-transfer regimes (Figure 2b and 2c). In the negative charge-transfer regime, the lower d band is pushed below the O 2p valence band, enabling charge transfer from the oxygen ligand to the Fe. The result is a so-called $d^n \underline{\text{L}}$ configuration ($\underline{\text{L}} = \text{ligand hole}$), which corresponds to an effective Fe oxidation state of 3+. In general, the charge-transfer energy is defined as the energy cost of transferring an electron from the O 2p valence band to the Fe 3d band (with respect to band centers of mass), i.e., charge fluctuations of type $d^n \rightarrow d^{n+1} \underline{\text{L}}$.^{39,40} Negative charge-transfer energies consequently indicate that the ground state is shifted to the right-hand side of this reaction. Note that the different regimes shown in Figure 2 so far disregard the effects of covalent interactions between the Fe 3d and the O 2p orbitals since they reflect the crystal-field picture only. These can, for instance, lead to the disappearance of the characteristic “ e_g over t_{2g} ” pattern of the octahedral crystal-field splitting, as the e_g orbitals become more strongly stabilized by σ -type covalent bonds, resulting in a broader band with a lower center of mass than the t_{2g} band. The covalent interactions will be discussed in more detail in the following sections.

4. RESULTS

4.1. Electronic Structure of Cubic BaFeO_3 . We begin by elaborating the general characteristics of the electronic structure of BaFeO_3 , focusing on the orbital interactions between the Fe 3d and the O 2p orbitals. Figure 3 shows the calculated (projected) density of states (DOS) and (projected) crystal orbital Hamilton population (COHP) curves of cubic BaFeO_3 . The DOS is composed of two spin components, each accompanied by a COHP curve.

From the DOS, one can clearly recognize that Fe adopts a high-spin configuration. The minority spin (down) bands e_g^\downarrow and t_{2g}^\downarrow are considerably separated from the majority spin (up) bands e_g^\uparrow and t_{2g}^\uparrow by 6.9 eV (with respect to the band centers of mass of the Fe 3d spin bands). The Fermi level falls in the upper region of the O 2p bands which thus remain partially unoccupied. The COHP diagrams reveal the formation of covalent bonds between Fe and O by virtue of a bonding

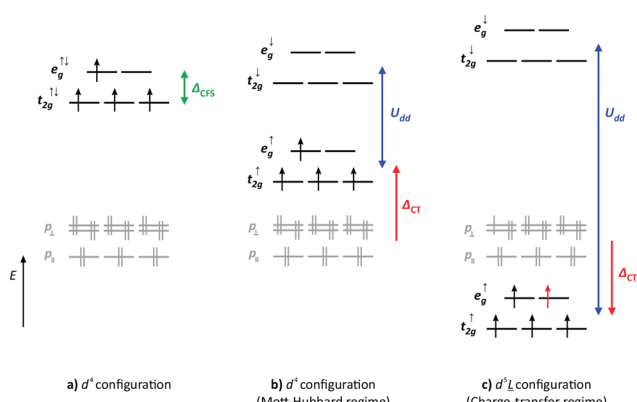


Figure 2. Possible ground state configurations of Fe d^4 in BaFeO_3 . Δ_{CFS} stands for octahedral crystal-field splitting, U_{dd} for the Coulomb and exchange repulsion, and Δ_{CT} for the charge-transfer energy.

of nominal electron configurations of d^4 (Fe^{4+}) and p^6 (O^{2-}) and assuming a high-spin configuration—typical for Fe in oxides—the model in Figure 2a would suggest a completely filled p band and a partially filled d band.

The electronic structure of iron-containing perovskites, however, often deviates from the conventional picture in Figure 2a by virtue of strong electron–electron interactions in the d orbitals of the metal, particularly, Coulomb repulsion and exchange interactions. The exchange interaction is often less intuitively understood but can be explained in terms of an effective nuclear charge felt by the electrons:³⁵ It follows from

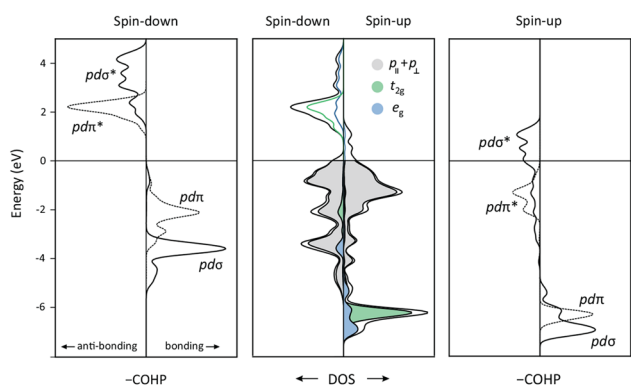


Figure 3. DOS (middle) and COHP curves (left, minority spin; right, majority spin) of cubic BaFeO_3 .

interaction ($\text{ICOHP} = -1.93 \text{ eV}$). This bonding interaction can be classified as $\text{pd}\sigma$ if the constituting orbitals are e_g and p_{\parallel} and as $\text{pd}\pi$ if the constituting orbitals are t_{2g} and p_{\perp} . As for the minority spin COHP (left panel in Figure 3), the antibonding states are formed primarily by d orbitals which remain unoccupied. The bonding states are formed by orbitals of p character which are occupied. This reflects a relatively stable configuration because the Fe–O bond is not destabilized by populated $\text{pd}\sigma^*$ and $\text{pd}\pi^*$ states. In the case of the majority spin COHP (right panel in Figure 3), the situation is reversed. The bonding states are now formed by orbitals of d character whereas the antibonding states are formed by orbitals of p character. The Fermi level thus falls in a $\text{pd}\sigma^*$ antibonding region with crystal orbitals of predominant p character. Figure 4 shows schematically the two different bonding patterns in the

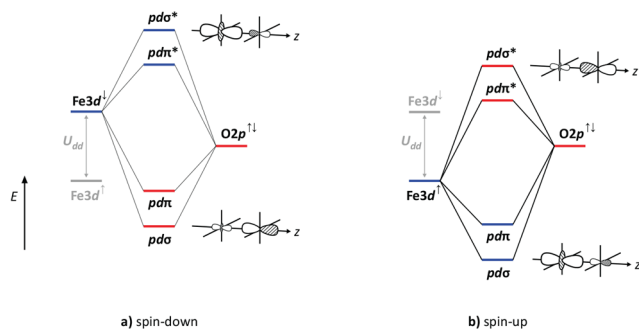


Figure 4. Schematic orbital diagrams for the covalent Fe–O bond involving spin-down orbitals (left) and spin-up orbitals (right). Note that on the left side the highest states have a predominant Fe 3d character, while on the right side they have a predominant O 2p character.

majority and minority spin components in a simplified orbital diagram. The figure highlights how the energy separation of majority and minority spin Fe 3d orbitals through Coulomb and exchange repulsion translates into different bonding patterns and causes the highest states in the majority spin component (Figure 4b) to have predominant O 2p character.

The characteristic pattern of the octahedral crystal-field splitting is preserved only in the unoccupied minority DOS where the e_g band is more destabilized through the formation of $\text{pd}\sigma^*$ bonds than the t_{2g} band through the formation of $\text{pd}\pi^*$ bonds. This pattern disappears in the majority DOS, where the d orbitals are involved in strong bonding

interactions. The states in the majority COHP are less pronounced than the states in the minority COHP (same scale on the x axis). This can be related to the fact that the majority spin orbitals are more contracted than the minority spin orbitals. In a high-spin configuration, the shielding of the nuclear charge in the majority spin orbitals is reduced and the electrons experience a stronger electron–nuclear attraction, which contracts the respective spin–orbitals. This reduces the pd interaction and results in less pronounced peaks in the majority spin COHP—a common phenomenon in spin-polarized systems because the more (less) diffuse minority (majority) spin orbitals contribute more (less) to covalent bonding. The integrated COHP up to the Fermi level yields -1.93 eV per Fe–O bond for both spin components together (-1.25 eV for minority spin orbitals, -0.68 eV for majority spin orbitals). The pd interaction in BaFeO_3 is composed of -0.40 eV (58%) per $\text{pd}\sigma$ bond and -0.29 eV (42%) per $\text{pd}\pi$ bond (see Table 1).

Table 1. Electronic Properties of Cubic BaFeO_3

	BaFeO ₃
$a/\text{\AA}$	4.015
$\Delta_{\text{CS}}/\text{eV}$	0.85
U_{dd}/eV	6.85
$\Delta_{\text{CT}}/\text{eV}$	-3.52
d^{\dagger}/e	4.82
d^{\downarrow}/e	1.00
$\mu_{\text{eff}}/\mu_{\text{B}}$	4.7
Q_{Ba}/e	1.75
Q_{Fe}/e	1.64
Q_{O}/e	-1.13
IP/eV	6.1
ICOHP-(pdσ)/eV	-0.40
ICOHP-(pdπ)/eV	-0.29
ICOHP-(Fe–O)/eV	-1.93

^a Δ_{CS} : crystal-field splitting. U_{dd} : energy cost for transferring an electron from the spin-up 3d band to the spin-down 3d band (with respect to band centers of mass) according to refs 39 and 40. Δ_{CT} : charge-transfer energy, energy cost for transferring an electron from the O 2p band to the Fe 3d band.^{39,40} d^{\dagger} , d^{\downarrow} : d-band population. μ_{eff} : effective magnetic moment given by $\mu_{\text{eff}} = g\sqrt{S(S+1)}$, where $g \approx 2$ and $S = (d^{\dagger} - d^{\downarrow})/2$.⁴¹ Q : Mulliken atomic charges. ICOHP: crystal orbital Hamilton population integrated up to the Fermi level. Fe–O ICOHP includes pdσ, pdπ, and interactions between the O 2s and the Fe 3p orbitals.

Comparing the DOS in Figure 3 with the schematic energy level diagrams in Figure 2, a strong similarity with the charge-transfer regime can be recognized. In fact, the relevant quantities U_{dd} and Δ_{CT} as extracted from the DOS with respect to the band centers are summarized in Table 1. Note that the values are given with respect to the band centers of mass which, in the case of the Fe 3d bands, are slightly off the main peaks at ~ -6 (spin up) and ~ 2 eV (spin down) due to minor contributions in the realm of the O 2p valence band. The extracted quantities clearly characterize BaFeO_3 as a negative charge-transfer material according to the definition in the literature.^{39,40} The Mulliken gross orbital populations are $d^{5.82}$ and $p^{5.23}$. They deviate significantly from the nominal electron configurations of d^4 and p^6 , which is, at least in part, due to the mixed ionic–covalent character of the Fe–O bond, as evidenced by the COHP curves in Figure 3. On the other

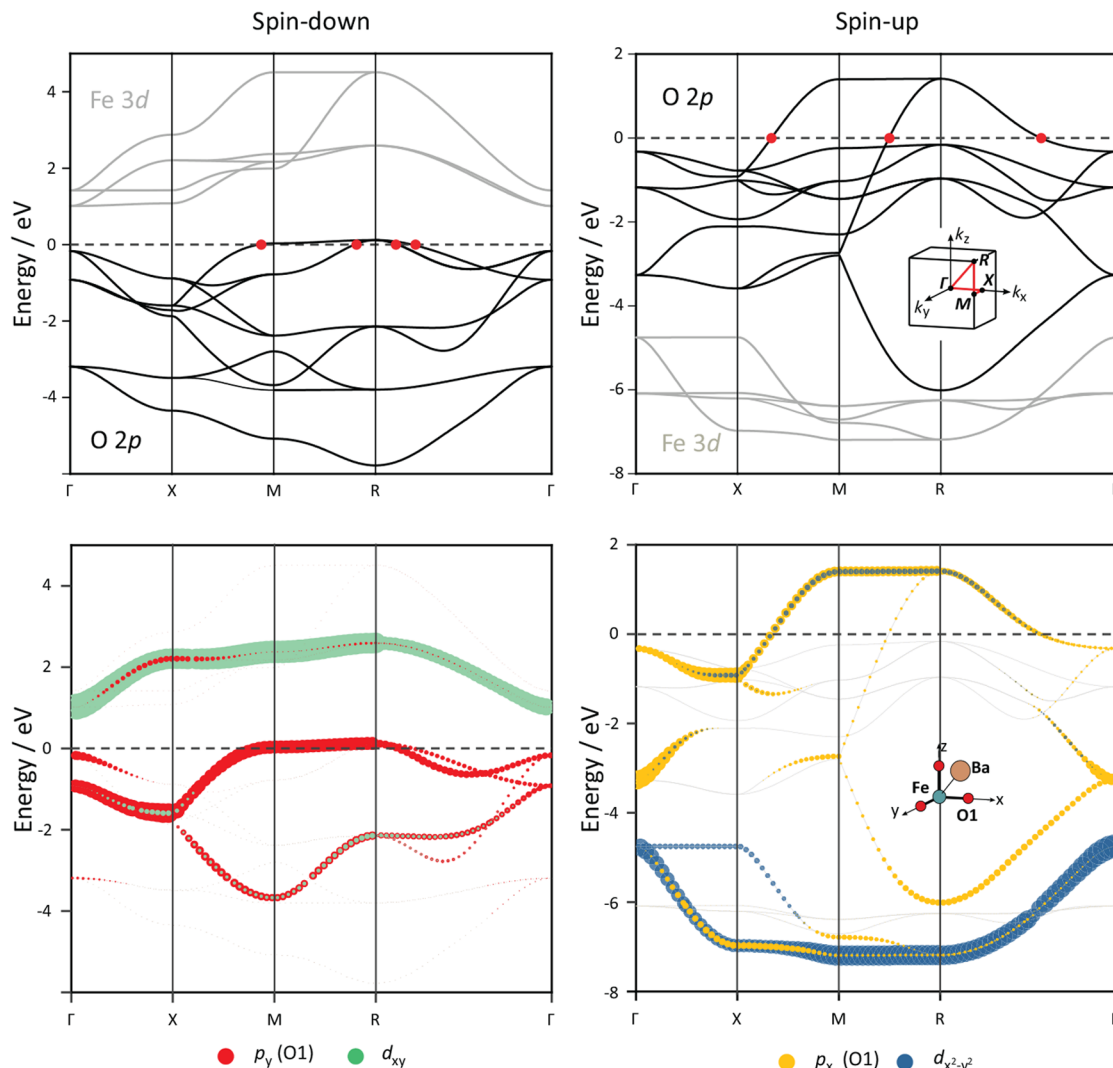


Figure 5. Band structures and fat-band plots of minority spin (left) and majority spin (right) components of BaFeO_3 .

hand, these orbital populations are the fingerprint of the charge transfer from the O ions to the Fe ion. The resulting electron configuration of $d^{5.82}$ is strongly reminiscent of a d^5L configuration. A value greater than 5 stems from the combination of negative charge transfer and a covalent Fe–O bond. The calculated Mulliken charges are $\text{Ba}^{+1.75}\text{Fe}^{+1.64}\text{O}_3^{-1.13}$. In conclusion, BaFeO_3 can be characterized as a high-spin, virtually half-metallic (disregarding the minute but noticeable DOS at the Fermi level in the minority spin component), electronically (hole) conducting, negative charge-transfer material. The COHP at the Fermi level reveals that the electron holes are partially delocalized in antibonding $\text{pd}\sigma^*$ crystal orbitals.

For comparison, we also calculated the total energy and electronic structure of hexagonal BaFeO_3 (space group $P6_3/mmc$). The total energy of the hexagonal phase is 0.07 eV per formula unit lower than the cubic phase, in line with the fact that the hexagonal structure of BaFeO_3 is experimentally the most stable one. The analysis of the projected COHP provides a natural explanation for that; the average Fe–O ICOHP in the hexagonal phase is more negative than that in the cubic phase (-2.00 eV in the hexagonal phase vs -1.93 eV in the cubic phase). This means that the coexistence of both corner-

and face-sharing $[\text{FeO}_6]$ octahedra in the hexagonal phase is able to strengthen the Fe–O covalent bond in BaFeO_3 . A plot of the DOS and COHP curves of the hexagonal phase analogous to Figure 3 can be found in section B of the Supporting Information.

Having established the general characteristics of the electronic structure through analysis of the DOS and COHP curves, we proceed with the cubic phase of BaFeO_3 by exploring the identified ligand holes in the band structure (Figure 5). In the minority spin band structure, only a few bands cross the Fermi level, which account for 10% of the total hole concentration per unit cell. In order to analyze the character of these bands, we make use of the so-called fat-band technique, where individual bands are plotted with a certain color and line width according to the type and mixing coefficient of some chosen atomic orbital to that band. Hence, the orbital source of a certain band is directly obvious in k space. The fat-band plot featuring one p_\perp orbital and the d_{xy} orbital is depicted in Figure 5, bottom, showing that the bands crossing the Fermi level in the minority spin part have predominant p_\perp character and that the p_\perp orbitals mix with the t_{2g} orbitals to form $\text{pd}\pi$ bonds. The strongest mixing occurs at the X point, where coefficients reach 80% d_{xy} and 20% p_\perp in

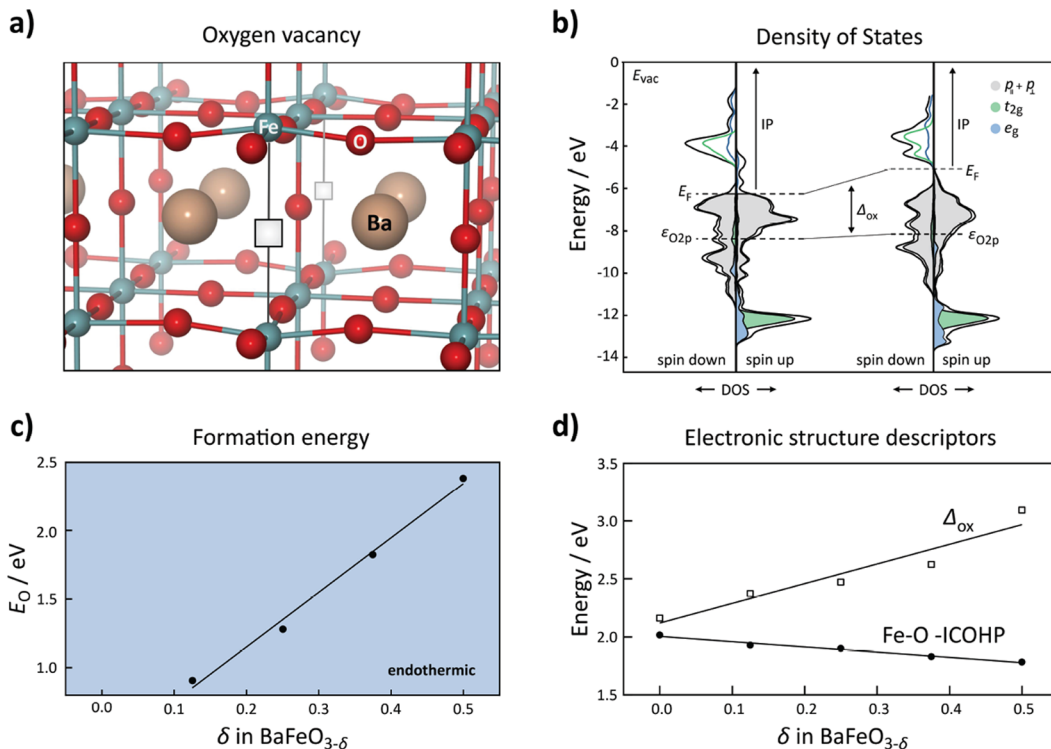


Figure 6. (a) Optimized atomic structure in the vicinity of an oxygen vacancy in a $2 \times 2 \times 2$ supercell. (b) DOS of oxidized BaFeO_3 (left) and reduced $\text{BaFeO}_{2.5}$ (right); see Supporting Information D for the band alignment technique. (c) Oxygen vacancy formation energy as a function of oxygen vacancy concentration. Each data point represents the average of three supercell configurations; see Supporting Information E. Data taken from ref 16. (d) Evolution of Δ_{ox} and average Fe–O ICOHP.

the unoccupied band at 2 eV. The formation of $\text{pd}\pi$ bonds is also evidenced by the dispersion of the t_{2g} bands, reaching a bandwidth of 1.6 eV.

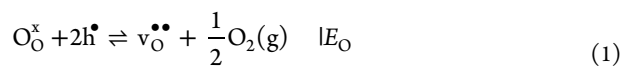
In the majority spin band structure, on the other hand, there are two bands crossing the Fermi level; the unoccupied states of these bands correspond to 90% of the total hole concentration. Notably, only two bands are responsible for the vast majority of the electron holes and, as such, the electronic conductivity in BaFeO_3 . When it comes to the even more disperse σ -type interactions, the fat-band plot featuring a p_{\parallel} orbital and the $d_{x^2-y^2}$ orbital is shown in Figure 5, bottom. The unoccupied states have a mixed p_{\parallel} - e_g character with a predominant contribution from the p_{\parallel} orbitals. From the COHP curve in Figure 3, it was concluded that these orbital interactions are antibonding. The fact that the p_{\parallel} orbitals are involved in antibonding interactions leads to two competing effects:

- (i) The axial crystal field at the oxygen lattice sites stabilizes the p_{\parallel} orbitals more than the p_{\perp} orbitals. In the absence of covalent interactions between the p and the d orbitals (e.g., at the Γ point), the p_{\parallel} COs will therefore lie below the p_{\perp} COs.
- (ii) The formation of $\text{pd}\sigma^*$ bonds destabilizes the p_{\parallel} bands more than the formation of $\text{pd}\pi^*$ bonds destabilizes the p_{\perp} bands, as a simple consequence of orbital topology. In the case of strong covalency, the p_{\parallel} -dominated bands will therefore be at higher energy than the p_{\perp} COs.

Indeed, at the Γ point, the p_x orbital contributes mostly to a lower lying band at ~ 3 eV. On leaving the Γ point, a $\text{pd}\sigma^*$ bond is established as indicated by the mixing of the p_x and $d_{x^2-y^2}$ orbitals between the Γ and the X points. The system tries

to counteract the destabilizing effect of the populated $\text{pd}\sigma^*$ states from -3 to -2 eV by pushing the p_x contribution to a band of higher energy at ~ 1 eV and eventually to an unoccupied band where it no longer destabilizes the system. This important result means that the bands crossing the Fermi level are mixtures of p_{\parallel} and e_g orbitals which have antibonding character. The unoccupied band at ~ 1 eV is composed of 80% $p_x + p_y$ and 20% $d_{x^2-y^2}$. The $\text{pd}\sigma$ bonding leads to a significant dispersion of the respective bands reaching a bandwidth of 2.5 eV for the e_g -dominated bands. The bandwidth for the p_{\parallel} -dominated bands is 4.7 eV due to the strong mixing with the p_{\perp} bands.

4.2. Formation of Oxygen Vacancies. The formation of oxygen vacancies in $\text{BaFeO}_{3-\delta}$ is characterized by substantial electronic and structural perturbation effects. Investigations of oxygen nonstoichiometric supercells by DFT¹⁶ showed that the square pyramidal $[\text{FeO}_5]$ polyhedra surrounding the oxygen vacancy contract with their equatorial oxygen ions relaxing slightly into the vacancy, see Figure 6a. (As a consequence of the lattice distortion, the supercell dimensions become noncubic with $a \neq b \neq c$.) Oxygen vacancies (denoted by v_O^{2-}) are formed according to reaction 1, where neutral oxygen is released into the atmosphere, with electrons of the former oxygen ion annihilating electron holes (h^{\bullet}).



Here, we make use of the Kröger–Vink notation⁴¹ where a subscript indicates the occupied lattice site and a superscript the relative charge with respect to the perfect crystal (\bullet = positive charge, $'$ = negative charge). In this context, v_O^{2-}

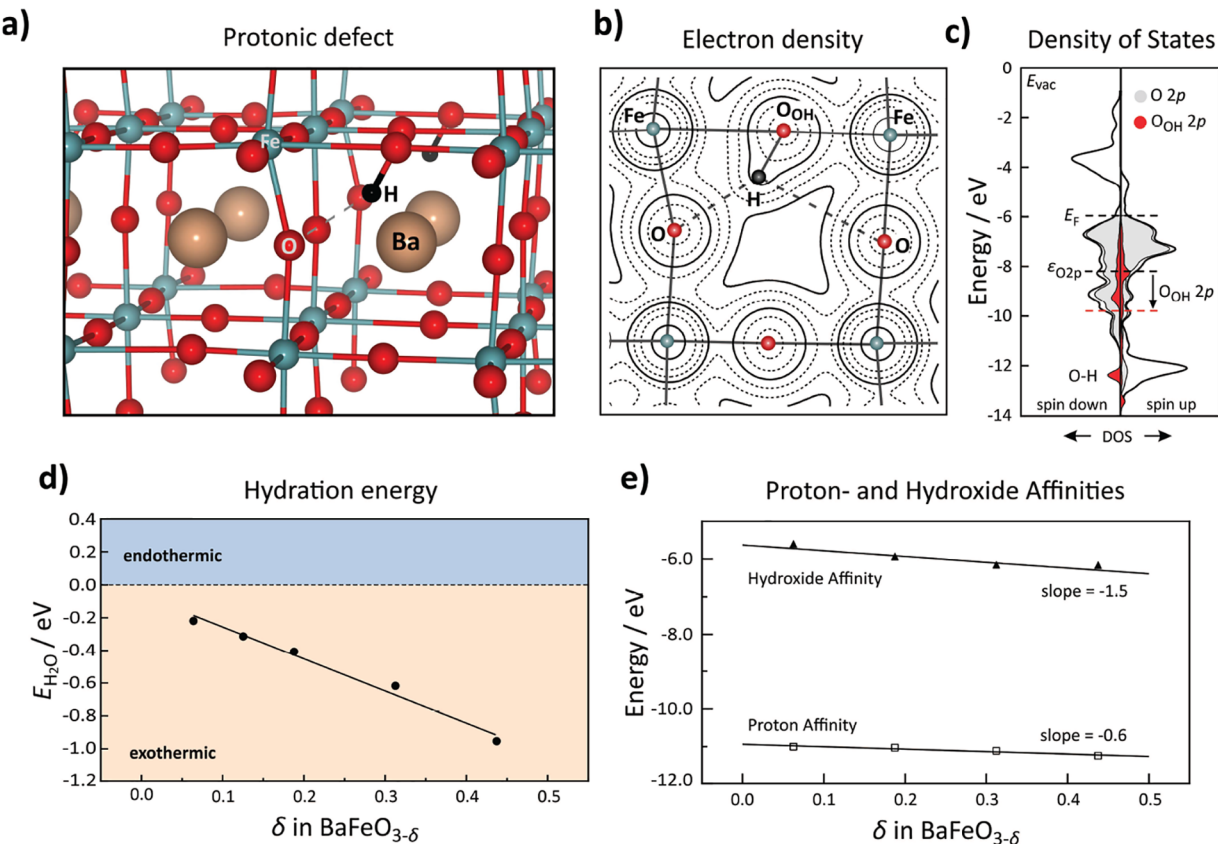


Figure 7. (a) Optimized atomic structure in the vicinity of a protonic defect in a $2 \times 2 \times 2$ supercell. (b) Contour map of the electron density distribution in $\text{Ba}_8\text{Fe}_8\text{O}_{24}\text{H}$; contour lines are drawn according to $10^{-2+\frac{n}{3}} e \text{ bohr}^{-3}$; bold lines correspond to 2×10^n with $n = -2, -1, 0$. (c) DOS curve of $\text{Ba}_8\text{Fe}_8\text{O}_{24}\text{H}$; H 1s states are multiplied by a factor of 10 and O_{OH} states by a factor of 5 for better visibility. (d) Hydration energy as a function of oxygen vacancy concentration. Each data point represents the average of the three lowest energy supercell configurations; see Supporting Information E. Data taken from ref 16. (e) Evolution of proton and hydroxide affinities as a function oxygen vacancy concentration; see Supporting Information for these calculations.

describes a vacancy at an oxygen lattice site that is doubly positively charged relative to a regular O^{2-} ion, i.e., has an absolute charge of zero. As a result of reaction 1, the Fermi level in BaFeO_3 rises with respect to the O 2p band center of mass (Figure 6b). Note that the small DOS at the top of the O 2p valence band implies that the position of the Fermi level is very sensitive to changes in the oxygen stoichiometry. In the reduced state, the O 2p band becomes fully occupied and the Fermi level resides in a very small band gap. Further reduction would lead to an occupation of Fe 3d minority spin orbitals. As a consequence of annihilating ligand holes, the average Mulliken atomic charge of the oxygen ions becomes more negative from $-1.13 e$ in the oxidized state (BaFeO_3) to $-1.32 e$ in the reduced state ($\text{BaFeO}_{2.5}$).

Regarding the oxygen vacancy formation as a function of vacancy concentration (Figure 6c) according to reaction 1, we observe the same trend as that in the experiments: The vacancy formation energy increases with increasing concentration of oxygen vacancies, specifically from 0.9 eV at $\delta = 0$ to 2.4 eV at $\delta = 0.5$. To explain this variation, we analyzed the electronic structures of various defective supercells and quantified the change in the Fermi level position relative to the O 2p band center of mass (Δ_{ox}) as well as the Fe–O ICOHP as a measure of the Fe–O bond strength (Figure 6d). As expected, Δ_{ox} increases continuously with increasing concentration of vacancies, thereby increasing the energetic

cost of further vacancy formation. On the other hand, the increased energy requirements associated with the higher Fermi level are counterbalanced by a decrease in the Fe–O bond strength as the concentration of vacancies rises. In particular, the average Fe–O ICOHP becomes less negative from -2.02 eV in the oxidized state to -1.78 eV in the reduced state, as shown in Figure 6. This results, on one hand, from the lattice expansion that accompanies oxygen vacancy formation (see ref 16) and the associated increased Fe–O bond lengths. On the other hand, the weakening of the Fe–O bond results from populating the $\text{pd}\sigma^*$ antibonding states at the Fermi level. To verify the latter, we performed an “artificial reduction” of BaFeO_3 , where we kept the oxygen stoichiometry and lattice parameters fixed and used a positive background charge to compensate for electrons added to the system (see section C in the Supporting Information for details). We then calculated the Fe–O ICOHP as a function of the number of added electrons to investigate how a population of $\text{pd}\sigma^*$ states at the Fermi level affects the Fe–O bond strength (at constant volume). Indeed, it turns out that populating the electron holes in BaFeO_3 leads to a softening of the Fe–O bond, highlighting the importance of COHP analyses in understanding the redox behavior of the material. The weakening of the Fe–O bond reduces the energetic cost of cleaving the Fe–O bonds required to remove an oxygen ion from the crystal. Eventually, the decrease in the Fe–O bond strength is overcompensated

by the increased energy requirements to move the electrons of the former oxygen ion from the center of the O 2p band to the Fermi level. This translates into a net increase in the energy required to form an oxygen vacancy and could explain the change in oxygen formation energy observed here for BaFeO₃ and also for other iron-containing perovskites.

For comparison, oxygen vacancy formation was also calculated for hexagonal BaFeO₃. This structure contains different oxygen sites (O1 and O2, see Figure 1) that are associated with different O 2p band centers of mass of −2.34 (O1) and −2.48 eV (O2) (relative to the Fermi level) and, as such, different Δ_{ox} . The oxygen vacancy formation energies of these oxygen ions are 0.72 (O1) and 0.96 eV (O2), respectively, and thus exhibit the same trend with Δ_{ox} (see section B in the Supporting Information for details).

The findings in this article also provide quantitative evidence for the itinerant electron model,⁴² in which the increase in vacancy formation energy in the La_{0.8}Sr_{0.2}CoO_{3−δ} system was argued to stem from an increasing Fermi level without taking into account the evolution of the Fe–O bond strength, oxygen ion charge, or absolute position of the O 2p band. In fact, the correlation between the oxygen vacancy formation energy and Δ_{ox} is valid not only within a particular system—as demonstrated in this article for BaFeO₃—but also across different materials (at least for the first vacancy introduced in a given supercell).⁴³ Trends between the oxygen vacancy formation energy and the cation composition of the perovskite host are discussed, e.g., in refs 43 and 44.

4.3. Dissociative H₂O Absorption. In equilibrium with ambient water vapor, iron-containing perovskites exhibit a moderate propensity for the dissociative absorption of water in their bulk. The reaction involves the dissociation of an adsorbed H₂O molecule into a proton and hydroxide ion followed by their incorporation into the bulk where the hydroxide ion fills an oxygen vacancy and the proton is attached to a regular oxygen ion (reaction 2).



The formed protonic defects (hydroxide ion on an oxygen ion site, OH_O[•]) give rise to proton conductivity at intermediate temperatures (300–700 °C) since a proton can easily be transferred to a neighboring oxygen ion.^{5,45} Figure 7a shows the equilibrium proton geometry in BaFeO₃, characterized by a typical O–H bond lengths of approximately 1 Å and a significant tilt to a neighboring oxygen ion favoring strong hydrogen bonding. Protonic defects also induce a significant perturbation of the local electronic structure. Figure 7b shows a contour map of the electron density distribution around a protonic defect in BaFeO₃. The proton is largely immersed in the electron cloud of the oxygen ion, leading merely to a bulge at the outer rim of the electron density of the oxygen ion. Between O and H in the hydroxyl group a slight accumulation of electron density can be noticed, indicating the formation of a covalent bond. The formation of the covalent bond is clearly visible in the DOS. Figure 7c shows that O–H bond formation leads to a distinct energetically low-lying state stemming from O 2p and H 1s mixing at ∼12.5 eV. In addition, O–H bond formation also leads to a downward shift in the other O 2p states of the respective O ion that are not directly involved in the O–H bond.

Figure 7d shows the energy change of reaction 2 for BaFeO₃ as a function of oxygen vacancy concentration. The reaction energy becomes subsequently more negative with an increasing

concentration of oxygen vacancies. This confirms similar experimentally observed trends in the literature¹⁴ and provides further evidence for detrimental interactions between electron holes and protons. With less holes present in the crystal (i.e., more oxygen vacancies), the perovskite host becomes more susceptible toward proton uptake via reaction 2. To understand this detrimental interaction between the electron holes and the proton interstitials, we make use of a recently developed formalism that allows quantifying the proton and hydroxide affinity using first-principles calculations.^{46,50} The idea is to split $E_{\text{H}_2\text{O}}$ into the invariant gas-phase water dissociation energy ($\text{H}_2\text{O} \rightarrow \text{H}^+ + \text{OH}^-$ with $\Delta E = 16.9$ eV) and the incorporation of H⁺ (proton affinity) and OH[−] (hydroxide affinity) into the solid oxide according to reactions 3 and 4.



Figure 7e shows the evolution of these ion affinities as a function of oxygen vacancy concentration in BaFeO₃. Both the proton and the hydroxide affinities become more negative for higher oxygen vacancy concentrations, with the slope of the hydroxide affinity being markedly steeper with −1.5 as compared to −0.6 for the proton affinity. This indicates that the decrease in hydration energy can be attributed largely to a more negative hydroxide affinity. A higher O ion charge in the reduced state seems to increase the energy gain upon incorporating an OH[−] from the gas phase, possibly via increased electrostatic interactions with the adjacent cations. These findings also allow us to derive a more general hypothesis, namely, that p-type electronic conductors in general have less negative hydration energies when the electron holes have a dominating O 2p character, since this leads to less negative hydroxide (and proton) affinities. By decreasing the ligand hole concentration—either through doping with redox-inactive cations (which also induce lattice distortions) or by reducing the material—the oxygen ion negative charge is subsequently increased. As a result, the electrostatic potential at the O site becomes stronger and the hydroxide affinity more negative. The proton affinity, on the other hand, decreases only moderately with increasing oxygen vacancy concentration, as can be seen in Figure 7e. This results from the analysis of the (three) most stable proton sites in a supercell of given oxygen stoichiometry.

Within one supercell, however, the proton affinity can vary significantly when considering not only the three most stable proton sites. It is particularly noteworthy that the oxygen ion opposite to an oxygen vacancy has a significantly less negative proton affinity. Figure 8 shows that the proton affinity correlates with the O 2p band centers of mass of the unprotonated oxygen ions, highlighting the importance of electronic structure descriptors in understanding the variations in the proton affinities of the lattice oxygen ions. Small deviations from this correlation occur because the proton affinity is also sensitive toward cases of very strong (weak) hydrogen bonding that can result in more (less) negative proton affinities than expected from the O 2p band center of mass.

5. CONCLUSIONS

The electronic structure and defect chemistry of cubic BaFeO₃ were calculated using DFT and analyzed in terms of local

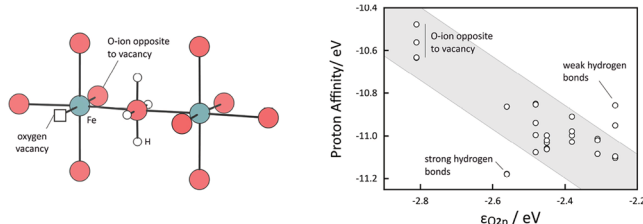


Figure 8. (Left) Atomic structure of $\text{BaFeO}_{3-\delta}$ featuring one oxygen vacancy and four possible proton sites around one oxygen ion. (Right) Proton affinities of one specific $\text{Ba}_8\text{Fe}_8\text{O}_{22}$ supercell as a function of O 2p band centers of mass in the dry state (i.e., prior to protonation).

atomic orbitals, which allowed for a chemically intuitive interpretation. The main results of these calculations can be summarized by the following points.

- (1) Cubic BaFeO_3 is a high-spin, virtually half-metallic, negative charge-transfer material with a dominating $d^5\text{L}$ configuration, as suggested by ref 36 and confirmed with X-ray spectroscopic studies on thin films^{8–10} as well as a density functional study²⁵ that identified cubic BaFeO_3 as a negative charge-transfer material
- (2) Chemical bonding analysis showed that the Fe–O bond has a significant covalent contribution and that the chemically active orbitals at the Fermi level (and ligand holes) have an antibonding $\text{pd}\sigma^*$ character. Specifically, the ligand holes are delocalized in Fe–O covalent bonds with an approximately 80% share at the oxygen ions.
- (3) The oxygen vacancy formation energy in BaFeO_3 increases as a function of the oxygen vacancy concentration due to a rising Fermi level at which electrons from the removed oxygen are accommodated. This effect outweighs a concomitant decrease in the Fe–O bond strength with oxygen vacancy concentration as shown by the Fe–O ICOHP.
- (4) The calculations confirm the experimental finding that a higher concentration of electron holes lowers the perovskite's propensity for the dissociative H_2O absorption. In BaFeO_3 , the hydration energy becomes more negative from ~-0.2 to ~-1.0 eV with an increasing concentration of oxygen vacancies from $\delta = 0$ to 0.5.
- (5) Analyses of the proton and hydroxide affinities of oxygen in nonstoichiometric $\text{BaFeO}_{3-\delta}$ revealed that the more negative hydration energies largely result from more negative hydroxide affinities. The proton affinity of the oxygen ions opposite an oxygen vacancy is much higher than that compared to other oxygen ions; this correlates with a much more negative O 2p band center of mass of the oxygen opposite the vacancy.

The present work highlights the interdependence of the electronic structure and defect chemistry of a material. Since in BaFeO_3 electron holes are largely associated with oxygen ions that are defect chemically active—through the formation of oxygen vacancies and as proton binding sites—the defect chemistry of BaFeO_3 is very sensitive toward changes in the electron hole concentration. Assigning classical oxidation states (Fe^{4+} , O^{2-}) is therefore an oversimplification, insufficient to explain the complex defect chemical behavior. In fact, the oxidation state of the iron, in particular, should be rather considered as 3+. The hole delocalization to the oxygen states

is also expected to affect the oxide ion and proton mobility. Finally, we emphasize the importance of the theoretical procedure with supercell calculations using a plane wave basis in VASP and a posteriori projection onto an auxiliary basis set of local atomic orbitals in LOBSTER. We were able to process a large number of defective supercells without sacrificing the ability to apply classical concepts of chemical bonding in terms of covalency and ionicity. Understanding the interplay between the electronic structure and the defect chemistry is moreover key to optimizing mixed proton–electron conducting oxides for protonic ceramic fuel and electrolyzer cells.

ASSOCIATED CONTENT

Supporting Information

The Supporting Information is available free of charge at <https://pubs.acs.org/doi/10.1021/acs.jpcc.2c02545>.

Jahn–Teller effect in BaFeO_3 , hexagonal phase of BaFeO_3 , artificial reduction, calculation of ionization potentials, supercell configurations, and calculation of proton and hydroxide affinity (PDF)

AUTHOR INFORMATION

Corresponding Author

M. F. Hoedl – Max Planck Institute for Solid State Research, 70569 Stuttgart, Germany; orcid.org/0000-0003-3166-6772; Email: m.hoedl@fkf.mpg.de

Authors

C. Ertural – Chair of Solid State and Quantum Chemistry, Institute of Inorganic Chemistry, RWTH Aachen University, 52056 Aachen, Germany

R. Merkle – Max Planck Institute for Solid State Research, 70569 Stuttgart, Germany; orcid.org/0000-0003-3811-8963

R. Dronskowski – Chair of Solid State and Quantum Chemistry, Institute of Inorganic Chemistry, RWTH Aachen University, 52056 Aachen, Germany; orcid.org/0000-0002-1925-9624

J. Maier – Max Planck Institute for Solid State Research, 70569 Stuttgart, Germany; orcid.org/0000-0003-2274-6068

Complete contact information is available at: <https://pubs.acs.org/10.1021/acs.jpcc.2c02545>

Funding

Open access funded by Max Planck Society.

Notes

The authors declare no competing financial interest.

ACKNOWLEDGMENTS

We thank Eugene Kotomin and Denis Gryaznov for fruitful discussions and proofreading of the manuscript. Computational resources of the High-Performance Computing Center Stuttgart (HLRS, project 12939 DEFTD) are gratefully acknowledged.

REFERENCES

- (1) Chen, G.; Feldhoff, A.; Weidenkaff, A.; Li, C.; Liu, S.; Zhu, X.; Sunarso, J.; Huang, K.; Wu, X.-Y.; Ghoniem, A.; et al. Roadmap for Sustainable Mixed Ionic-Electronic Conducting Membranes. *Adv. Funct. Mater.* **2022**, 32, 2105702.

- (2) Irvine, J.; Rupp, J.; Liu, G.; Xu, X.; Haile, S.; Qian, X.; Snyder, A.; Freer, R.; Eken, D.; Skinner, S.; et al. Roadmap on inorganic perovskites for energy applications. *J. Phys.: Energy* **2021**, *3*, 031502.
- (3) Merkle, R.; Maier, J. How is oxygen incorporated into oxides? A comprehensive kinetic study of a simple solid-state reaction with SrTiO_3 as a model material. *Angew. Chem., Int. Ed.* **2008**, *47*, 3874–3894.
- (4) Merkle, R.; Hoedl, M. F.; Raimondi, G.; Zohourian, R.; Maier, J. Oxides with Mixed Protonic and Electronic Conductivity. *Annu. Rev. Mater. Res.* **2021**, *51*, 461–493.
- (5) Zohourian, R.; Merkle, R.; Raimondi, G.; Maier, J. Mixed-conducting perovskites as cathode materials for protonic ceramic fuel cells: understanding the trends in proton uptake. *Adv. Funct. Mater.* **2018**, *28*, 1801241.
- (6) Papac, M.; Stevanović, V.; Zakutayev, A.; O'Hayre, R. Triple ionic–electronic conducting oxides for next-generation electrochemical devices. *Nat. Mater.* **2021**, *20*, 301–313.
- (7) Ding, X.; Gao, X.; Zhu, W.; Wang, J.; Jiang, J. Electrode redox properties of $\text{Ba}_{1-x}\text{La}_x\text{FeO}_{3-\delta}$ as cobalt free cathode materials for intermediate-temperature SOFCs. *International journal of hydrogen energy* **2014**, *39*, 12092–12100.
- (8) Bocquet, A.; Fujimori, A.; Mizokawa, T.; Saitoh, T.; Namatame, H.; Suga, S.; Kimizuka, N.; Takeda, Y.; Takano, M. Electronic structure of $\text{SrFe}^{4+}\text{O}_3$ and related Fe perovskite oxides. *Phys. Rev. B* **1992**, *45*, 1561.
- (9) Mizumaki, M.; Fujii, H.; Yoshii, K.; Hayashi, N.; Saito, T.; Shimakawa, Y.; Uozumi, T.; Takano, M. Electronic structure of BaFeO_3 studied by x-ray spectroscopy. *physica status solidi (c)* **2015**, *12*, 818–821.
- (10) Tsuyama, T.; Matsuda, T.; Chakraverty, S.; Okamoto, J.; Ikenaga, E.; Tanaka, A.; Mizokawa, T.; Hwang, H.; Tokura, Y.; Wadati, H. X-ray spectroscopic study of BaFeO_3 thin films: An Fe^{4+} ferromagnetic insulator. *Phys. Rev. B* **2015**, *91*, 115101.
- (11) Zohourian, R. Mixed-conducting perovskites as cathodes in protonic ceramic fuel cells: defect chemistry and transport properties. Ph.D. Thesis, University of Stuttgart, Stuttgart, 2018.
- (12) Gryaznov, D.; Merkle, R.; Kotomin, E.; Maier, J. Ab initio modelling of oxygen vacancies and protonic defects in $\text{La}_{1-x}\text{Sr}_x\text{FeO}_{3-\delta}$ perovskite solid solutions. *Journal of Materials Chemistry A* **2016**, *4*, 13093–13104.
- (13) Kuklja, M.; Mastrikov, Y.; Jansang, B.; Kotomin, E. The Intrinsic Defects, Disorder, and Structural Stability of $\text{Ba}_x\text{Sr}_{1-x}\text{Co}_y\text{Fe}_{1-y}\text{O}_{3-\delta}$ Perovskite Solid Solutions. *J. Phys. Chem. C* **2012**, *116*, 18605–18611.
- (14) Zohourian, R.; Merkle, R.; Maier, J. Bulk defect chemistry of PCFC cathode materials: discussion of defect interactions. *ECS Trans.* **2017**, *77*, 133.
- (15) Raimondi, G.; Giannici, F.; Longo, A.; Merkle, R.; Chiara, A.; Hoedl, M.; Martorana, A.; Maier, J. X-ray spectroscopy of $(\text{Ba}, \text{Sr}, \text{La})(\text{Fe}, \text{Zn}, \text{Y})\text{O}_{3-\delta}$ identifies structural and electronic features favoring proton uptake. *Chem. Mater.* **2020**, *32*, 8502–8511.
- (16) Hoedl, M.; Gryaznov, D.; Merkle, R.; Kotomin, E.; Maier, J. Interdependence of Oxygenation and Hydration in Mixed-Conducting $(\text{Ba}, \text{Sr})\text{FeO}_{3-\delta}$ Perovskites Studied by Density Functional Theory. *J. Phys. Chem. C* **2020**, *124*, 11780–11789.
- (17) Blöchl, P. E. Projector augmented-wave method. *Phys. Rev. B* **1994**, *50*, 17953–17979.
- (18) Kresse, G.; Hafner, J. Ab-initio molecular dynamics for liquid metals. *Phys. Rev. B* **1993**, *47*, 558–561.
- (19) Kresse, G.; Furthmüller, J. Efficiency of ab-initio total energy calculations for metals and semiconductors using a plane-wave basis set. *Comput. Mater. Sci.* **1996**, *6*, 15–50.
- (20) Kresse, G.; Furthmüller, J. Efficient iterative schemes for ab-initio total-energy calculations using a plane-wave basis set. *Phys. Rev. B* **1996**, *54*, 11169–11186.
- (21) Monkhorst, H.; Pack, J. Special points for Brillouin-zone integrations. *Phys. Rev. B* **1976**, *13*, 5188.
- (22) Pack, J.; Monkhorst, H. Special points for Brillouin-zone integrations—a reply. *Phys. Rev. B* **1977**, *16*, 1748.
- (23) Perdew, J. P.; Burke, K.; Ernzerhof, M. Generalized Gradient Approximation Made Simple. *Phys. Rev. Lett.* **1996**, *77*, 3865–3868.
- (24) Dudarev, S.; Botton, G.; Savrasov, S.; Humphreys, C.; Sutton, A. Electron-energy-loss spectra and the structural stability of nickel oxide: An LSDA+U study. *Phys. Rev. B* **1998**, *57*, 1505–1509.
- (25) Ribeiro, B.; Godinho, M.; Cardoso, C.; Borges, R.; Gasche, T. Self-doping and the role of oxygen vacancies in the magnetic properties of cubic $\text{BaFeO}_{3-\delta}$. *J. Appl. Phys.* **2013**, *113*, 083906.
- (26) Lee, Y.; Kleis, J.; Rossmeisl, J.; Morgan, D. Ab initio energetics of LaBO_3 (001) ($B = \text{Mn}, \text{Fe}, \text{Co}$, and Ni) for solid oxide fuel cell cathodes. *Phys. Rev. B* **2009**, *80*, 224101.
- (27) Baiyee, Z.; Chen, C.; Ciucci, F. A DFT+U study of A-site and B-site substitution in $\text{BaFeO}_{3-\delta}$. *Phys. Chem. Chem. Phys.* **2015**, *17*, 23511–23520.
- (28) Dronskowski, R.; Blöchl, P. Crystal orbital Hamilton populations (COHP): energy-resolved visualization of chemical bonding in solids based on density-functional calculations. *J. Phys. Chem.* **1993**, *97*, 8617–8624.
- (29) Deringer, V.; Tchougréeff, A.; Dronskowski, R. Crystal orbital Hamilton population (COHP) analysis as projected from plane-wave basis sets. *J. Phys. Chem. A* **2011**, *115*, 5461–5466.
- (30) Maintz, S.; Deringer, V.; Tchougréeff, A.; Dronskowski, R. Analytic projection from plane-wave and PAW wavefunctions and application to chemical-bonding analysis in solids. *Journal of computational chemistry* **2013**, *34*, 2557–2567.
- (31) Maintz, S.; Deringer, V.; Tchougréeff, A.; Dronskowski, R. LOBSTER: A tool to extract chemical bonding from plane-wave based DFT. *Journal of computational chemistry* **2016**, *37*, 1030–1035.
- (32) Ertural, C.; Steinberg, S.; Dronskowski, R. Development of a robust tool to extract Mulliken and Löwdin charges from plane waves and its application to solid-state materials. *RSC Adv.* **2019**, *9*, 29821–29830.
- (33) Nelson, R.; Ertural, C.; George, J.; Deringer, V.; Hautier, G.; Dronskowski, R. LOBSTER: Local orbital projections, atomic charges, and chemical-bonding analysis from projector-augmented-wave-based density-functional theory. *J. Comput. Chem.* **2020**, *41*, 1931–1940.
- (34) Ertural, C.; Stoffel, R.; Müller, P.; Vogt, C.; Dronskowski, R. First-Principles Plane-Wave-Based Exploration of Cathode and Anode Materials for Li-and Na-Ion Batteries Involving Complex Nitrogen-Based Anions. *Chem. Mater.* **2022**, *34*, 652–668.
- (35) Dronskowski, R. *Computational chemistry of solid state materials*; Wiley-VHC: Weinheim, New York, 2005.
- (36) Hayashi, N.; Yamamoto, T.; Kageyama, H.; Nishi, M.; Watanabe, Y.; Kawakami, T.; Matsushita, Y.; Fujimori, A.; Takano, M. BaFeO_3 : a ferromagnetic iron oxide. *Angew. Chem.* **2011**, *123*, 12755–12758.
- (37) Chakraverty, S.; Matsuda, T.; Ogawa, N.; Wadati, H.; Ikenaga, E.; Kawasaki, M.; Tokura, Y.; Hwang, H. BaFeO_3 cubic single crystalline thin film: A ferromagnetic insulator. *Appl. Phys. Lett.* **2013**, *103*, 142416.
- (38) Grey, I.; Li, C.; Cranswick, L.; Roth, R.; Vanderah, T. Structure Analysis of the 6H- $\text{Ba}(\text{Ti}, \text{Fe}^{3+}, \text{Fe}^{4+})\text{O}_{3-\delta}$ Solid Solution. *J. Solid State Chem.* **1998**, *135*, 312–321.
- (39) Zaanen, J.; Sawatzky, G.; Allen, J. Band gaps and electronic structure of transition-metal compounds. *Physical review letters* **1985**, *55*, 418.
- (40) Bisogni, V.; Catalano, S.; Green, R.; Gibert, M.; Scherwitzl, R.; Huang, Y.; Strocov, V.; Zubko, P.; Balandeh, S.; Triscone, J.; et al. Ground-state oxygen holes and the metal–insulator transition in the negative charge-transfer rare-earth nickelates. *Nat. Commun.* **2016**, *7*, 13017.
- (41) West, A. *Solid state chemistry and its applications*; John Wiley & Sons: Chichester, UK, 2014.
- (42) Kröger, F. *The chemistry of imperfect crystals*; North-Holland, 1964.
- (43) Lankhorst, M.; Bouwmeester, H. Determination of Oxygen Nonstoichiometry and Diffusivity in Mixed Conducting Oxides by

- Oxygen Coulometric Titration: II. Oxygen Nonstoichiometry and Defect Model for. *J. Electrochem. Soc.* **1997**, *144*, 1268.
- (44) Lee, Y.; Kleis, J.; Rossmeisl, J.; Shao-Horn, Y.; Morgan, D. Prediction of solid oxide fuel cell cathode activity with first-principles descriptors. *Energy Environ. Sci.* **2011**, *4*, 3966–3970.
- (45) Curnan, M.; Kitchin, J. Effects of concentration, crystal structure, magnetism, and electronic structure method on first-principles oxygen vacancy formation energy trends in perovskites. *J. Phys. Chem. C* **2014**, *118*, 28776–28790.
- (46) Kreuer, K. Proton-conducting oxides. *Annu. Rev. Mater. Res.* **2003**, *33*, 333–359.
- (47) Bjørheim, T.; Hoedl, M.; Merkle, R.; Kotomin, E.; Maier, J. Proton, hydroxide ion, and oxide ion affinities of closed-shell oxides: importance for the hydration reaction and correlation to electronic structure. *J. Phys. Chem. C* **2020**, *124*, 1277–1284.
- (48) Blanksby, S.; Ellison, G. Bond dissociation energies of organic molecules. *Accounts of chemical research* **2003**, *36*, 255–263.
- (49) Ruscic, B.; Wagner, A.; Harding, L.; Asher, R.; Feller, D.; Dixon, D.; Peterson, K.; Song, Y.; Qian, X.; Ng, C.; et al. On the enthalpy of formation of hydroxyl radical and gas-phase bond dissociation energies of water and hydroxyl. *J. Phys. Chem. A* **2002**, *106*, 2727–2747.
- (50) Smith, J.; Kim, J.; Lineberger, W. High-resolution threshold photodetachment spectroscopy of OH⁻. *Phys. Rev. A* **1997**, *55*, 2036.

□ Recommended by ACS

Correlation of Electrochemical Characteristics with Structural, Optical, and Electrical Properties in Tungsten-Doped Li₄Ti₅O₁₂ Anodes

Humaira S. Bhatti, Ghulam Ali, et al.

APRIL 14, 2023

THE JOURNAL OF PHYSICAL CHEMISTRY C

READ ↗

Hexagonal Tungsten Bronze H_{0.25}Cs_{0.25}Nb_{2.5}W_{2.5}O₁₄ as a Negative Electrode Material for Li-Ion Batteries

Etienne Le Calvez, Thierry Brousse, et al.

APRIL 10, 2023

CHEMISTRY OF MATERIALS

READ ↗

Compositionally Complex Perovskite Oxides for Solar Thermochemical Water Splitting

Dawei Zhang, Jian Luo, et al.

FEBRUARY 21, 2023

CHEMISTRY OF MATERIALS

READ ↗

High-Pressure, High-Temperature Studies of Phase Transitions in SrOsO_x—Discovery of a Post-Perovskite

Camilla Hjort Kronbo, Martin Bremholm, et al.

NOVEMBER 16, 2022

INORGANIC CHEMISTRY

READ ↗

Get More Suggestions >